respectively. Meanwhile, as shown in Fig. 8 and Table I, the range of the fluctuation of the walking speed (relative to the maximum speed) is decreasing, while the torso-inclination angle, α, is increasing.

V. Conclusion

In this study, we proposed a simple strategy, torso inclination, for fast walking in PAWs. We have simulated a PAW model and analyzed how the torso inclination affects its walking behavior. Although there is a reality gap between the simulation and the real robot's experimental results, both of them indicate that torso inclination can greatly increase the walking speed of PAWs by reducing the fluctuation of the instantaneous speed.

References

[1] J. Pratt,"Exploiting inherent robustness and natural dynamics in the control of bipedal walking robots," Ph.D. dissertation, Dept. Elect. Eng. Comput. Sci., Massachusetts Inst. Technol., Cambridge, MA, USA, 2000.
[2] C. Chevallereau, G. Abba, Y. Aoustin, F. Plestan, E. Westervelt, C. Canudas-deWit, and J. Grizzle, "Rabbit: A testbed for advanced control theory," *IEEE Control Syst.*, vol. 23, no. 5, pp. 57–79, Oct. 2003.
[3] K. Sreenath, H. Park, I. Poulakakis, and J. W. Grizzle, "Compliant hybrid zero dynamics controller for achieving stable, efficient and fast bipedal walking on MABEL," *Int. J. Robot. Res.*, vol. 30, no. 9, pp. 1170–1193, 2011.
[4] T. Geng, B. Porr, and F. Wörgötter, "Fast biped walking with a sensor-driven neuronal controller and real-time online learning," *Int. J. Robot. Res.*, vol. 25, no. 3, pp. 243–259, 2006.
[5] D. Hao, M. Zhao, and N. Zhang, "High-speed and energy-efficient biped locomotion based on virtual slope walking," *Auton. Robots*, vol. 30, no. 2, pp. 199–216, 2011.
[6] J. Dean and A. Kuo, "Elastic coupling of limb joints enables faster bipedal walking," *J. Roy. Soc. Interface*, vol. 6, no. 16, pp. 561–573, 2009.
[7] T. Geng and J. Q. Gan, "Planar biped walking with an equilibrium point controller and state machines," *IEEE/ASME Trans. Mechatronics*, vol. 15, no. 2, pp. 253–260, Apr. 2010.
[8] T. Wada, M. Ishikawa, R. Kitayoshi, I. Maruta, and T. Sugie, "Practical modeling and system identification of R/C servo motors," in *Proc. IEEE Int. Conf., Control Appl., Int. Symp. Intell. Control*, 2009, pp. 1378–1383.
[9] M. Garcia,"Stability, scaling, and chaos in passive dynamic gait models," Ph.D. dissertation, Dept. Mech. Eng., Cornell Univ., Ithaca, NY, USA, 1999.

Robotic Probing of Nanostructures inside Scanning Electron Microscopy

Zheng Gong, Brandon K. Chen, Jun Liu, and Yu Sun

***Abstract*—Probing nanometer-sized structures to evaluate the performance of integrated circuits (IC) for design verification and manufacturing quality monitoring demands precision nanomanipulation technologies. To minimize electron-induced damage and improve measurement accuracy, scanning electron microscopy (SEM) imaging parameters must be cautiously chosen to ensure low electron energy and dosage. This results in significant image noise and drift. This paper presents automated nanoprobing with a nanomanipulation system inside a standard SEM. We achieved SEM image denoising and drift compensation in real time. This capability is necessary for achieving robust visual tracking and servo control of nanomanipulators for probing nanostructures in automated operation. This capability also proves highly useful to conventional manual operation by rendering real-time SEM images that have little noise and drift. The automated system probed nanostructures on an SEM metrology chip as surrogates of electronic features on IC chips. Success rates in visual tracking and *Z*-contact detection under various imaging conditions were quantitatively discussed. The experimental results demonstrate the system's capability for automated probing of nanostructures under IC-chip-probing relevant electron microscope imaging conditions.**

***Index Terms*—Automated nanoprobing, drift compensation, image denoising, nanomanipulation system, scanning electron microscope (SEM).**

I. Introduction

Nanomanipulation inside scanning electron microscopes (SEMs) enables visual observation and physical interactions with objects at the submicrometer and nanometer scales. Applications range from nanomaterial characterization [1]–[4], to micro-nano device assembly [5], [6], to photonics [7], [8], and to biology research [9]. In addition, it has become the standard for the semiconductor industry to evaluate the performance of integrated circuitries (IC) via nanoprobing under electron microscopy imaging [10]. Nanoprobing inside the SEM allows needle probes to be precisely positioned on top of submicrometer-sized electrodes for direct electrical characterization, which is important for failure analysis, quality control, and process development for the semiconductor industry [11], [12].

During the nanoprobing process, SEM imaging conditions must be carefully controlled to ensure accurate probing and minimal electron beam-induced damage to the IC chip [13]. The electron dosage to the sample should be kept low by using low accelerating voltage and emission current and short irradiation time. Under these conditions, imaging resolution and signal-to-noise ratio are poor, and image drift is serious. SEM image drift refers to the movement of the entire image, caused by electron beam drift, charge drift on the specimen, and electromagnetic interference from the environment. In nanoprobing, image drift becomes particularly significant at high magnifications under low accelerating voltages, which must be compensated for. The constraint of short irradiation time also imposes pressure and high requirements in operation dexterity on the human operator, which can reduce the reliability and consistency of nanoprobing.

Automation at the nanometer scale rapidly progressed in the past few years. Automated nanomanipulation inside the SEM has been reported for nanoscaled material handling and characterization. Utilizing nanoprobes and microgripping tools, nanowires were visually identified, picked up, transferred, and characterized [14]–[16]. Nanomaterial-based field-effect-transistor biosensors were constructed via SEM-based nanomanipulation, which involves controlling nanoprobes to remove unwanted nanowires bridging the source and drain electrodes [17]. Automated manipulation of bio materials (single cells) under SEM imaging was also demonstrated [18]. These automation systems utilize visual servoing for precise positioning of an end-tool; thus, the automation performance depends heavily on the SEM imaging quality. In electron microscopy imaging, imaging quality is proportional to electron beam energy and dosage to the sample. For nanoprobing of electronic structures, where electron energy and dosage must be kept to minimum, automation must cope with the severely degraded images containing high noise and large image drift.

Manuscript received October 2, 2013; revised January 4, 2014. Date of publication January 27, 2014; date of current version June 3, 2014. This paper was recommended for publication by Guest Editor S. Martel and Editor B. J. Nelson upon evaluation of the reviewers' comments. This work was supported by the Natural Sciences and Engineering Research Council of Canada under a Strategic Projects Grant and by the Canada Research Chairs Program.

The authors are with the Advanced Micro and Nanosystems Laboratory, University of Toronto, Toronto, ON M5S 3G8, Canada (e-mail: zgong@mie.utoronto.ca; brandon.chen@utoronto.ca; ljun@mie.utoronto.ca; sun@mie.utoronto.ca).

Color versions of one or more of the figures in this paper are available online at http://ieeexplore.ieee.org.

Digital Object Identifier 10.1109/TRO.2014.2298551

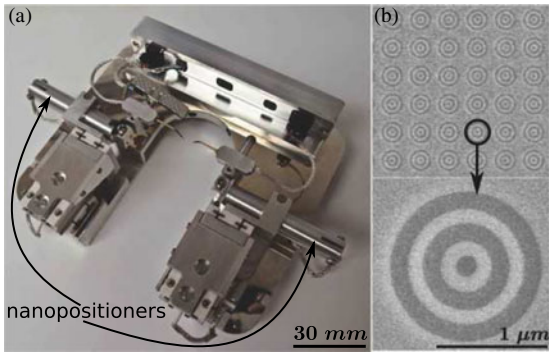

Fig. 1. (a) Nanomanipulation system. (b) Nanostructures on an SEM metrology chip used in nanoprobing experiments.

The majority of existing noise reduction methods are local smoothing filters such as the Gaussian smoothing model [19], neighborhood filtering [20], and anisotropic filtering [21]. Other algorithms such as total variation minimization [22], [23] use the calculus of variations for denoising images. In comparison, the nonlocal means (NL-means) method [24] is based on globally averaging all the pixels in an image and produces images with lower noise and with more details retained. The algorithm when implemented on central processing units (CPUs), however, is highly time-consuming and not suitable for real-time SEM image denoising/processing.

As to image-drift compensation, Cizmar *et al.* reported a correction technique that works with a large number of quickly taken frames, which are properly aligned and then composed into a single image [25]. This correction technique does not satisfy the real-time requirement for nanoprobing. Sutton *et al.* used two- dimensional (2-D) digital image correlation [26] for high accuracy measurements but not for real-time applications. Techniques were also developed for drift compensation in atomic force microscopy (AFM) imaging [27], [28]. Due to the fundamental differences in imaging principles, the AFM drift compensation techniques are not applicable to SEM imaging.

State-of-the-art nanoprobing is conducted manually by highly trained personnel, who carefully control nanomanipulator positions via joysticks and closely observe the SEM screen that displays images of poor quality and significant drift. This paper, for the first time, presents a nanomanipulation system (see Fig. 1) and automation techniques that together enable reliable automated nanoprobing of nanostructures inside the SEM. Compared with our previous nanomanipulation system, the new system integrates tubular nanopositioners that provide a motion range of tens of micrometers with subnanometer resolution and nonobservable vibration. Graphics processing unit (GPU)-accelerated real-time NL-means video denoising is achieved, which significantly increases the success rate of automated nanoprobing. Experimental evaluation of the proposed approaches are discussed. The realization of automated probing of nanostructures on SEM metrology chips is demonstrated. Compared with our conference paper [29], this paper provides additional details on technique implementation and nanoprobing results; furthermore, improved success rates of automated nanoprobing are presented.

II. System Design

A. Nanomanipulation System

Nanomanipulation systems typically use the same piezo stack to produce coarse motion (stick-slip mode) and fine motion (scanning mode). This configuration provides potentially unlimited coarse motion ranges with excellent static positioning capability. However, the high-frequency stick-slip piezo movements generate mechanical vibrations and can result in poor dynamic behavior. The vibration can be further amplified at the low-stiffness nanoprobes attached to the nanomanipulator, causing the delicate probe tip to "whip" around while moving. This can damage the probe tip and/or the sample. In the fine-motion mode, vibration is not existent; however, the motion range is typically rather limited (e.g., <5 μm).

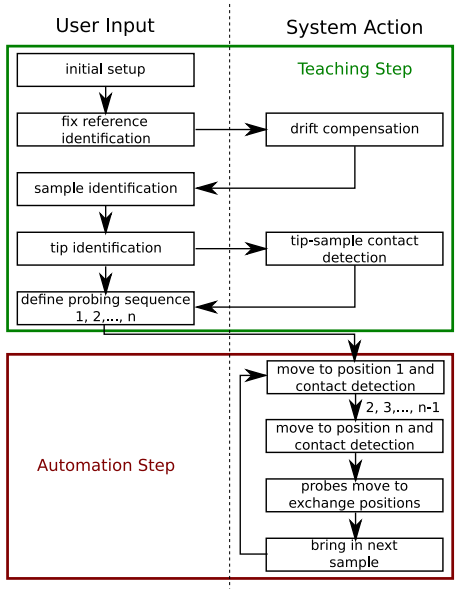

Fig. 2. Flow of the nanoprobing process.

To satisfy the stringent static and dynamic positioning requirements for nanoprobing, design modifications were made to our previously reported nanomanipulation system [30]. Similar to the previous system, the new system [see Fig. 1(a)] consists of two independent 3-degree-of-freedom (DOF) manipulators mounted on an SEM load-lock compatible carrier. A tubular nanopositioner, illustrated in Fig. 3, similar to an atomic force microscopy piezo scanner is added to each manipulator. It was constructed by connecting a piezo tube in series with a piezostack, covered by a metallic housing for shielding. The piezo tube provides radial bending motion and the piezo stack provides axial extension. These nanopositioners, shown in Fig. 1, have subnanometer motion resolution and a motion range that is at least an order of magnitude larger than the magnitude of vibration from coarse positioning. The overall nanomanipulation system has a motion range of 10 mm provided by the piezo stack; a fine motion range of tens of micrometers with subnanometer resolution and nonobservable vibration. System characterization was conducted through subpixel tracking based on SEM imaging, as previously described in [30].

B. Overall Process of Nanoprobing

The nanoprobing process is divided into two steps. The teaching step involves the user who defines the automation task, followed by full automation of nanoprobing on specified locations on a sample.

In the teaching step (see Fig. 2), the human operator first uses joysticks or our program interface to bring the two probe tips and the sample into the field of view and field of depth. The drift compensation algorithm is initiated by selecting a fixed feature that is stationary on the sample. Target structures on the sample for probing are then selected via computer mouse clicking and stored. The automated Z-contact

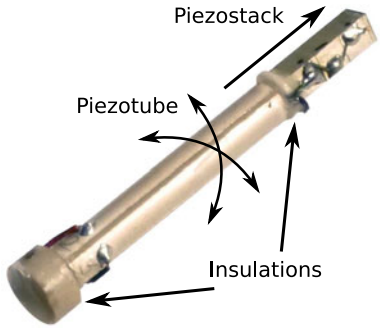

Fig. 3. Nanopositioner design, consisting of piezotube for radial bending, and piezostack for axial extension.

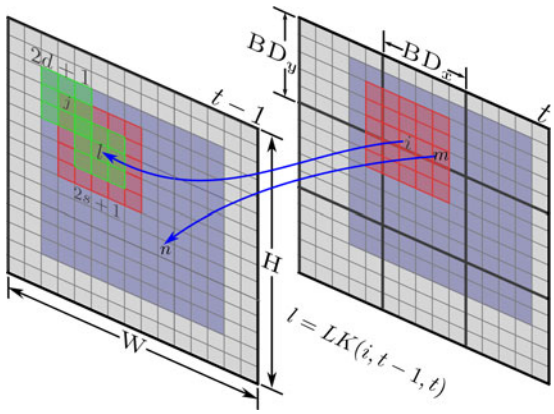

Fig. 4. NL-means filter and implementation on GPU.

detection algorithm is initiated and brings both probe tips to contact the sample. The contact detection algorithm is based on detecting the sliding motion of the probe tip on the sample upon contact [31]. The teaching process ends with the user defining the sequence of probing targets for each of the two probes.

In the automation step (see Fig. 2), the system controls automatically the two nanoprobes to move in *XY* to each of the predefined probing targets in sequence and execute *Z*-contact detection to establish probe-sample contact. When the nanoprobes move to the next targets for probing, they are lifted (∼200 nm) by the system, moved in *XY* to the next target, and then contact the targets via automated Z-contact detection.

When all targets are probed within the field of view, the nanoprobes are retracted to their original positions in 3-D. The system controls the SEM stages to move the sample and bring new probing targets into the field of view. The complete nanoprobing flow is repeated.

C. NL-Means Denoising Implemented on GPU

In the NL-means algorithm [24], given a noisy image $v = \{v(i)|i \in I\}$, the denoised value $NL[v](i)$, for a pixel i, is computed as a weighted average of all the pixels in the search window (red window in Fig. 4) of size $(2s+1) \times (2s+1)$, according to

$$NL[v](i) = \sum_{j \in I} w(i,j)v(j) \tag{1}$$

where the family of weights $\{w(i,j)\}_j$ depends on the similarity between pixels i and j (green window in Fig. 4).

The above equation describes single image NL-means denoising. Since nanoprobing requires the handling of image sequences (versus singe image), due to the temporal correspondence of image sequence, more similar patches can be found than just searching within the current single frame. By extending the single image approach to image sequence NL-means, better denoising results can be achieved. In practice, robust optical flow-based motion estimation is often used to establish reliable temporal correspondence [32]. With the estimated motion flow, the denoised result $NL[v](i,t)$ of frame $v(i,t)$ is

$$NL[v](i,t) = \sum_{k=t-F}^{t} \tau^{t-k} \sum_{j \in I} w(i,j,k,t)v(j,k) \tag{2}$$

where τ is a coefficient controlling temporal decay and is set to 0.9 in experiments. F is number of backward frames and set to 3. The family of weights $\{w(i,j,k,t)\}_{j,k}$, satisfying $0 \le w(i,j,k,t) \le 1$ and $\sum_k \sum_j w(i,j,k,t) = 1$, is defined as

$$w(i,j,k,t) = \frac{1}{Z(i)} e^{-\frac{\|v(\mathcal{N}_{LK(i,k,t)},k) - v(\mathcal{N}_j,k)\|^2_{2,\alpha}}{h^2}} \tag{3}$$

where pixel $LK(i,k,t)$ at frame k corresponds to pixel i at frame t, which is determined with the Lucas-Kanade method [32]. $Z(i)$ is the normalizing constant

$$Z(i) = \sum_k \sum_j e^{-\frac{\|v(\mathcal{N}_{LK(i,k,t)},k) - v(\mathcal{N}_j,k)\|^2_{2,\alpha}}{h^2}}. \tag{4}$$

$\mathcal{N}_l$ denotes a square neighborhood window (green window in Fig. 4) of fixed size $(2d+1) \times (2d+1)$ and centered at a pixel l. $\| \quad \|^2_{2,\alpha}$ is the Euclidean distance weighted by a Gaussian kernel g of standard deviation α. In our implementation, it is replaced with the classical Euclidean distance $\| \quad \|^2_2$ since the classical Euclidean distance is a reliable measure for the comparison of images in a window [33]. The value of h controls the decay of the exponential function.

Although the NL-means filter can produce better denoising results compared with other algorithms (comparison results discussed later), it consumes significant computing power because of the large amount of data it fetches. For each pixel i at frame t, $F(2s+1)^2$ number of weights $\{w(i,j,k,t)\}_{j,k}$ need to be calculated. To calculate each weight $\{w(i,j,k,t)\}_{j,k}$, additional $(2d+1)^2$ number of weights $\mathcal{N}_l$ need to be determined. Hence, the overall computational complexity of the NL-means algorithm to produce one filtered frame is $O(FWHs^2d^2)$, where W and H are image width and height, respectively. For standard CPU implementation of the NL-means filter, it costs at least several seconds to process a 640 × 480 image.

With the rapid evolution of the GPU technology, GPU processing is well suited to address problems that can be expressed as data-parallel computations since the same function is executed on many data elements in parallel. The NL-means filter belongs to this class of problem. Thus, we, for the first time, implemented the algorithm on GPU to achieve real-time denoising/filtering of SEM images via the graphics programming language Compute Unified Device Architecture (CUDA) [34].

In CUDA, the GPU serves as a processing device for the CPU. The CPU calls kernel functions that run on the GPU to perform tasks in a high number of parallel threads. All threads are organized into multiple independent blocks. As illustrated in Fig. 4, the threads are divided into 2-D blocks, with each block containing $BD_x \times BD_y$ number of threads. The entire frame has $W \times H$ number of pixels, and each pixel is filtered by one thread. Hence, the total number of blocks is $\lceil \frac{W}{BD_x} \rceil \times \lceil \frac{H}{BD_y} \rceil$.

In our implementation of the NL-means algorithm, parallel reduction was conducted to fully exploit parallelism. The memory bandwidth was

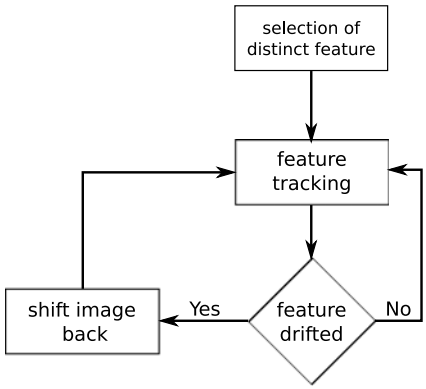

Fig. 5. Flow of drift compensation.

maximized by prefetching data to shared memory. The shared memory is a dedicated on-chip user-controllable memory for fast read/write, which is shared by every thread in a block. By loading all the operands required by the threads in a block into shared memory from the GPU global RAM, the subsequent large amount of instructions will only fetch data from the shared memory. Hence, the data transfer cost was dramatically reduced considering the huge bandwidth difference between the on-chip shared memory and the off-chip global RAM.

Since each block has only $BD_x \times BD_y$ threads, and each thread filters one pixel, only a small number of pixels from the image sequence are fetched to shared memory. In the NL-means filter, in order to determine the denoised value for a pixel i, all the pixels j in the search window centered at pixel i and all the pixels in the neighborhood window centered at each pixel j must be fetched. This means that for the threads lying on the border of a block, such as pixel i in Fig. 4, extra pixels around the block are required to compute denoised value $NL[v](i)$. For an image sequence, similar patches are searched for in the previous F frames. The patch size is affected by the maximal difference $|\Delta \mathbf{z}|$ in optical flow between adjacent frames for pixels within a block, such as pixel i and m in Fig. 4. Since image sequences are collected under the fast scanning mode (20 Hz), $|\Delta \mathbf{z}|$ is no more than 6 based on experimental trials. Therefore, overall $F(BD_x + 2s + 2d + |\Delta \mathbf{z}|)^2$ pixels (purple square in Fig. 4) are required by a 2-D block consisting of $BD_x \times BD_y$ threads and fetched into shared memory to reduce the data transfer cost of the subsequent operations.

D. Drift Compensation

To compensate for SEM image drift, visual tracking is conducted. In the initialization step of nanoprobing, a distinct stationary feature on the sample is manually selected. In the automation steps, in each captured SEM image, the selected feature is tracked to verify whether drift occurs, and the system performs drift compensation. The procedure is illustrated in Fig. 5. Feature tracking determines the effectiveness of drift compensation.

Correlation-based template matching [35] is an algorithm for object tracking and position estimation in noisy images. The orientation and scale estimation involves a long computation time and can endanger the real-time tracking performance of the algorithm. This was not a concern in our system because the orientation of the nanoprobe is fixed.

The tracking task for image drift compensation is to determine the position of a given pattern in an image f. Let $f(x, y)$ denote the intensity value of the image with a size of $M_x \times M_y$ at the point $(x, y), x \in 0, \ldots, M_x - 1, y \in 0, \ldots, M_y - 1$. The pattern is represented by a given template t with a size of $N_x \times N_y$. A common way to calculate the position $(u_{\text{pos}}, v_{\text{pos}})$ of the pattern is to evaluate the normalized cross correlation coefficient, γ at each point (u, v) for f and the template t, which has shifted by u steps in the x direction and by v steps in the y direction. The normalized cross-correlation coefficient is

$$\gamma = \frac{\sum_{x,y}(f(x,y) - \overline{f}_{u,v})(t(x-u, y-v) - \overline{t})}{\sqrt{\sum_{x,y}(f(x,y) - \overline{f}_{u,v})^2 \sum_{x,y}(t(x-u, y-v) - \overline{t})^2}} \quad (5)$$

where $\overline{f}_{u,v}$ denotes the mean value of $f(x, y)$ within the area of the template t shifted to (u, v)

$$\overline{f}_{u,v} = \frac{1}{N_x N_y} \sum_{x=u}^{u+N_x-1} \sum_{y=v}^{v+N_y-1} f(x, y). \quad (6)$$

Similarly, the notation $\overline{t}$ is the mean value of the template t.

TABLE I
NANOMANIPULATION SYSTEM SPECIFICATIONS

dimensions	complete system	$110 \times 93 \times 32\ mm^3$
	manipulator	$36 \times 21 \times 22\ mm^3$
	nanopositioner	$42.5 \times 8.5 \times 8.5\ mm^3$
coarse positioning	range	$10\ mm$
	encoder resolution	$2\ nm$
fine positioning	radial bending range	$\pm 30\ \mu m$
	radial bending resolution	$1.2\ nm$
	axial extension range	$10\ \mu m$
	axial extension resolution	$1.2\ nm$

III. EXPERIMENTAL RESULTS

A. Nanomanipulation System Characterization

Table I summarizes the main specifications of the nanomanipulation system. Detailed characterization of the coarse positioning system was reported in [30]. Nanopositioner characterization was conducted using SEM imaging at high magnifications. With the driving electronics used in the system, the achievable motion resolution should be subnanometer. However, the actual measurement result as summarized in Table I was limited by the imaging resolution of the SEM.

B. Characterization of SEM Image Noise and Drift

Experiments were conducted to quantify SEM image drift and noise under various imaging conditions. Image drift is defined as random movements of the entire SEM image, caused by shifting of the electron beam due to external disturbances (e.g., magnetic field change). Noise is defined as random variations in each pixel. The combined effect of drift and noise can be quantified by tracking a stationary object/feature over time. To decouple the drift and noise effect, two stationary objects in close proximity were tracked simultaneously, and the difference between the two was determined to be the noise level. The tracking accuracy was quantified by tracking a feature on a still image and determined to be 0.03 ± 0.16 pixel.

Fig. 6 summarize the effect of varying magnifications and varying accelerating voltages on SEM image noise and drift. A total of 500 frames of SEM images were collected under the fast scanning mode (20 Hz) for quantifying noise and drift under magnifications from 1000× to 80 000×. Another 500 frames of fast-scanned images were collected to measure noise and drift under accelerating voltages from 1 to 20 kV. For each of the 500 frames collected, objects were visually tracked, and the magnitude of their displacements compared with the previous frame was determined. The data quantitatively show that

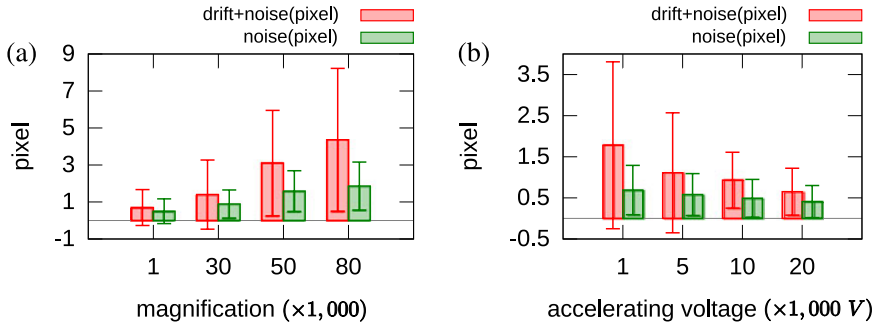

Fig. 6. (a) SEM noise and drift under different magnifications. Accelerating voltage: 1 kV; emission current: 10 μA for all testing. The results are obtained from tracking 500 frames for each magnification. (b) SEM noise and drift under different accelerating voltages. Emission current: 10 μA; magnification: 35 000× for all testing. The results are obtained from tracking 500 frames for each accelerating voltage. The error bars represent ±1 standard deviation.

TABLE II
GPU AND CPU PROCESSING TIME OF NL-MEANS FILTERING

search window	GPU sec/frame	CPU sec/frame	speed-up ratio
7×7	0.005	2.89	577.27
11×11	0.012	6.72	560.01
21×21	0.039	19.82	508.13
31×31	0.211	83.91	397.68

lower accelerating voltage and higher magnification, as required in IC structure probing, induce increased image noise and drift [see video].

C. Real-Time SEM Image Denoising

Nanoprobing requires the use of lower accelerating voltages and a reasonably high magnification; hence, images have high noise and drift. The GPU accelerated NL-means filter was implemented on a standard computer (Intel Core i7 3.6GHz CPU, 3GB DDR3 RAM, NVidia GTX560 GPU with 1GB global memory and 48kB on-chip shared memory per block). For NVidia GTX 560 GPU, each block can contain at most 1024 threads; therefore, we set the block size to 32×32. In this way, by storing pixels as one byte data, $(32 + 2 * 10 + 2 * 3 + 6)^2 \times 3 = 12\,288$ bytes are fetched into shared memory, which avoids the overfill of the 48-kB shared memory.

In the NL-means denoising algorithm, d is the similarity window radius. It was found in our experiments that a 7×7 similarity window was large enough to be robust to noise and small enough to maintain details. Table II shows the NL-means filter processing time of a 640×480 SEM image using different search window sizes, computed using both GPU and CPU. It takes more than 2 s for the latest CPU (e.g., Intel Core i7 3.6 GHz) to process one noisy image, while 0.04 s or shorter per frame is required for real-time applications. The results show that GPU processing time is 300–500 times faster than the CPU in our system. The 21×21 search window was chosen since it provides a frame rate of 25 frames per second and in the meanwhile provides satisfactory denoising result. The parameter h controls the degree of filtering. A larger h value removes noises but also image details, and a smaller h value preserves details but also noises. For our application, h was experimentally set to 10σ. The standard deviation of the added noise σ, was calculated for each SEM image frame.

Fig. 7(a) shows an image captured in the fast scanning mode (20 Hz) and Fig. 7(b) in slow scanning mode (0.5 Hz). The rest of the images in Fig. 7 are denoising results using the image sequence NL-means algorithm [see Fig. 7(c)], single image NL-means algorithm [see Fig. 7(d)], and two other popular filtering algorithms: *K*-nearest neighborhood [see Fig. 7(e)] and total variation [see Fig. 7(f)]. To quantitatively compare the results from these filtering algorithms, the slow scanned image [see Fig. 7(b)] was used as a reference to compute the peak signal-to-noise ratio (PSNR) values. The comparison results demonstrated that image sequence NL-means filtering achieves the highest PSNR score. While it is more effective in reducing SEM image noise, it also retains detailed information (e.g., edge) to the highest degree.

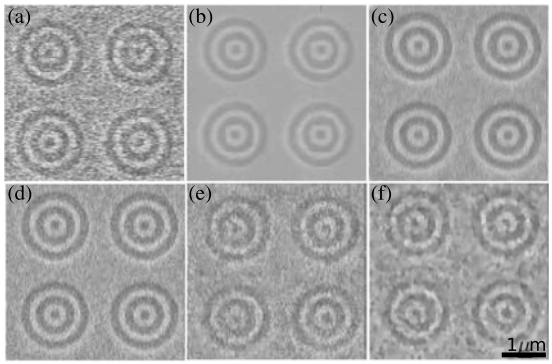

Fig. 7. Comparison of filtering results using different denoising algorithms. (a) Raw image captured in fast scanning mode (20 Hz). (b) Image captured in slow scanning mode (0.5 Hz). (c)–(f) Images filtered with image sequence NL-means algorithm (PSNR = 21.91); single image NL-means algorithm (PSNR = 21.78); *K*-nearest neighborhood algorithm (PSNR = 21.05); and total variation algorithm (PSNR = 20.74).

D. Visual Tracking of Nanoprobe Tips

Nanoprobe tips were mounted on the nanomanipulation system. For evaluating visual tracking performance, SEM imaging conditions were set to 1-kV accelerating voltage, 10 μA emission current, and 10 mm working distance to simulate IC probing-relevant situations. The SEM used in the experiments was a Hitachi-S4800.

Visual tracking was conducted for visual servo control of the nanoprobes in the *XY* directions and also for vision-based contact detection in the *Z*-direction. Tracking success rates were quantified for the following scenarios: 1) without drift compensation or noise reduction; 2) with only noise reduction; 3) with only drift compensation; and 4) with both drift compensation and noise reduction.

Visual tracking of probe tips in the *XY* directions was repeated 20 times under magnifications of (1000×)−(80 000×) for each of the four previously mentioned scenarios. The manipulator movement speed was scaled according to changes in magnification in order to ensure that the probes move at a constant speed (100 pixels/s) under all magnifications. *XY* visual tracking was considered successful when

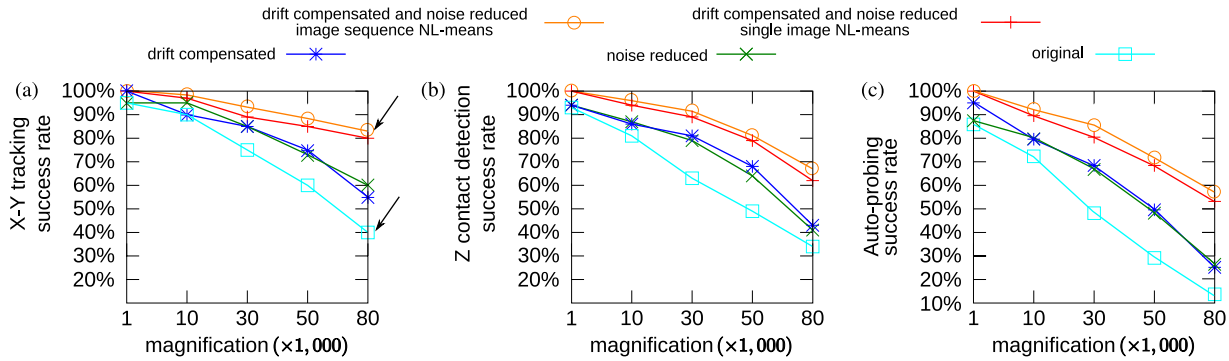

Fig. 8. Success rates under various imaging magnifications. (a) *XY* visual tracking of nanoprobes. (b) Z-contact detection. (c) Automated nanoprobing.

the probe stays within ±3 pixels of the predefined path and reaches the final destination. As summarized in Fig. 8(a), at low magnifications, similar tracking success rates were obtained in all four scenarios because image noise and drift are both less severe. However, at higher magnifications (e.g., 80 000×), combined drift compensation and noise reduction resulted in a 40% higher success rate than directly performing nanoprobe tracking in the raw images [success rates: 83% versus 40%, arrow labelled in Fig. 8(a)].

For nanoprobing, probe tips must physically contact target structures on a sample. In vision-based contact detection, reliable tracking of nanoprobe tips is critical for detecting the sliding motion that starts to be present in the image plane when the probe tips contact the sample. For each test in our experiments, the probes were lowered from approximately 20 μm above the sample. Contact detection was considered successful when the probe contacted the sample surface and slid for less than 3 pixels from when the tip first made contact with the sample. All other cases were considered a failure. Under each magnification, testing was repeated 20 times.

Fig. 8(b) summarizes the results of automated *Z*-contact detection under the four scenarios. Image filtering and drift compensation are necessary for achieving high success rates in *Z*-contact detection. It needs to be noted that there is a sharp drop in *Z*-contact detection success rate comparing magnifications of 50 000× and 80 000× for all four scenarios. This occurred because the depth of field under 80 000× is smaller than the separation between the nanoprobe tip and the sample. Therefore, only the tip or the sample (but not both) can be within focus initially. As the probe tip descended toward the sample and hence into focus, failure rates in probe tip template matching became higher.

The complete nanoprobing operation consists of *XY* visual tracking, followed by *Z*-contact detection. Fig. 8(c) summarizes the success rate of automated nanoprobing conducted under different image magnifications. As expected, the nanoprobing success rate is approximately equal to the success rate of *XY* visual tracking multiplied by the success rate of the *Z*-contact detection procedure. Compared with single image NL-means filtering, image sequence NL-means filtering improved the success rate of automated nanoprobing by an additional 3% on average. Fig. 9 summarizes the success rates of automated nanoprobing using different denoising algorithms. The results further demonstrate the advantage of image sequence NL-means filtering.

E. Nanoprobing

An SEM metrology chip from MetroBoost was used for nanoprobing tests. The sample contains hundreds of submicrometer-sized patterns that are metallic features suitable for probing tests. Compared with IC chips, these samples do not require lengthy sample preparation (e.g., decapsulation). The selected sample pattern on the chip consists

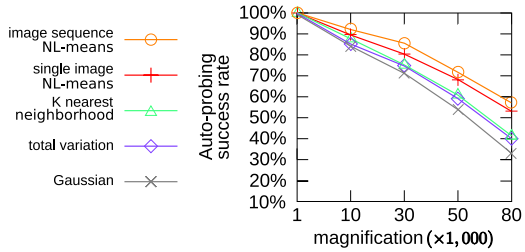

Fig. 9. Success rate of automated nanoprobing using different denoising algorithms.

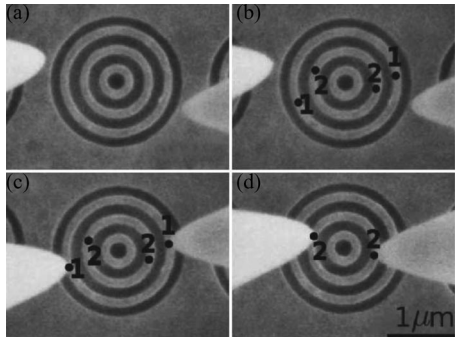

Fig. 10. Automated nanoprobing under 40 000× magnification. The two nanoprobes were visually servoed in the XY directions to reach user-defined locations (1-1 and 2-2). The system automatically landed the probes on the targets using vision-based *Z*-contact detection.

TABLE III
COMPARISON OF MANUAL AND AUTOMATED NANOPROBING

Operator	I	II	III	Automated
Time(s)	57.2±7.0	46.5±4.1	86.2±12.3	15.3±1.7

of concentric circles with line width of 130 nm separated by 125 nm spacing. The sample was mounted on the SEM stage and can be rotated independently from the nanomanipulation system. Tungsten nanoprobes were cleaned with potassium hydroxide and hydrofluoric acid for removing surface oxide, resulting in a tip radius < 100 nm. The probes were mounted on each of the two nanomanipulators and were electrically grounded.

Fig. 10 shows a sequence of screenshots taken during the automated nanoprobing process. The nanoprobing task was conducted at a magnification of 40 000×. Three skilled human operators each executed the same probing task 20 times, and the operation speed was compared with automated operation, as summarized in Table III. Excluding the man-

ual teaching steps, automated nanoprobing took approximately 15 s to probe four points (labeled 1-1 and 2-2 in Fig. 10). This automated probing speed is at least three times higher than the manual probing speed of a highly skilled operator. The SEM image drift compensation and noise reduction techniques implemented in our system enabled reliable automated nanoprobing; and also proved highly useful to manual probing by rendering higher quality SEM images in real time [see video].

Failed nanoprobing occurred when a sudden image shift happened due to the environmental change in a magnetic field (e.g., on-off of motors and passing by of train/streetcars). The installation of a field cancellation system is necessary for mitigating this issue. A sudden image shift or change in brightness could also happen when the sample and probe are not at the same electric potential, causing a large electric discharge when the two make contact. Furthermore, the probe can also change in brightness depending upon its location relative to the secondary electron detector, which can create shadowing effects. Our ongoing study aims to tackle these challenges to enhance the automated nanoprobing system.

IV. Conclusion

Nanoprobing electronic features necessitates the use of low accelerating voltage, low emission current, and short irradiation time in imaging in order to minimize electron beam-induced damage to IC circuits. In the meanwhile, high imaging magnifications are required for accurately probing nanometer-sized target structures. These conditions result in high noise and large drift in real-time electron microscopy imaging, posing challenges to both manual operation by skilled operators and the implementation of automated nanoprobing. This paper presented a system for automated nanoprobing inside a standard SEM. The system is capable of 10 mm travel in three axes with motion resolutions better than 1 nm. Techniques for denoising SEM images and for compensating for SEM image drift were developed. Visual servoing and position control embedded in the system enabled precise positioning of nanoprobes. Experimental results demonstrated that the system is capable of performing automated probing on nanostructures with a high success rate, at a speed at least three times higher than skilled operators.

Acknowledgment

The authors would like to thank Hitachi High-Technologies Canada Inc. for their technical assistance.

References

[1] M. Yu, O. Lourie, M. Dyer, K. Moloni, T. Kelly, and R. Ruoff, "Strength and breaking mechanism of multiwalled carbon nanotubes under tensile load," *Science*, vol. 287, no. 5453, pp. 637–640, 2000.

[2] T. Fukuda, F. Arai, and L. Dong, "Assembly of nanodevices with carbon nanotubes through nanorobotic manipulations," *Proc. IEEE*, vol. 91, no. 11, pp. 1803–1818, Nov. 2003.

[3] D. J. Bell, L. Dong, B. J. Nelson, M. Golling, L. Zhang, and D. Grützmacher, "Fabrication and characterization of three-dimensional InGaAs/GaAs nanosprings," *Nano Lett.*, vol. 6, no. 4, pp. 725–729, 2006.

[4] Y. Zhu, F. Xu, Q. Qin, W. Y. Fung, and W. Lu, "Mechanical properties of vapor-liquid-solid synthesized silicon nanowires," *Nano Lett.*, vol. 9, no. 11, pp. 3934–3939, 2009.

[5] H. Dai, J. Hafner, A. Rinzler, D. Colbert, and R. Smalley, "Nanotubes as nanoprobes in scanning probe microscopy," *Nature*, vol. 384, no. 6605, pp. 147–150, 1996.

[6] J. Li, Y. Zhang, S. To, L. You, and Y. Sun, "Effect of nanowire number, diameter, and doping density on nano-fet biosensor sensitivity," *ACS Nano*, vol. 5, no. 8, pp. 6661–6668, 2011.

[7] K. Aoki, H. Miyazaki, H. Hirayama, K. Inoshita, T. Baba, K. Sakoda, N. Shinya, and Y. Aoyagi, "Microassembly of semiconductor three-dimensional photonic crystals," *Nat. Mater.*, vol. 2, pp. 117–121, 2003.

[8] H. Chen, C. He, C. Wang, M. Lin, D. Mitsui, M. Eguchi, T. Teranishi, and S. Gwo, "Far-field optical imaging of a linear array of coupled gold nanocubes: Direct visualization of dark plasmon propagating modes," *ACS Nano*, vol. 5, no. 10, pp. 8223–8229, 2011.

[9] M. Ahmad, M. Nakajima, M. Kojima, S. Kojima, M. Homma, and T. Fukuda, "Nanofork for single cells adhesion measurement via ESEM-nanomanipulator system," *IEEE Trans. NanoBioscience*, vol. 11, no. 1, pp. 70–78, Mar. 2012.

[10] R. Stallcup and K. Inoue, "Nanoprobing sram bit cells with high-speed pulses," *Electron. Device Failure Anal.*, vol. 11, no. 4, pp. 22–27, 2009.

[11] D. Martin, R. Desplats, G. Haller, P. Nouet, and F. Azaïs, "Automated diagnosis and probing flow for fast fault localization in IC," *Microelectron. Rel.*, vol. 44, no. 911, pp. 1553–1558, 2004.

[12] H. Park, S.-Y. Han, W.-S. Lee, C.-H. Jeon, S. Sohn, K. Chae, S. Yamada, W. Yang, and D. Park, "Electrical failure analysis methodology for dram of 80nm era and beyond using nanoprober technique," in *Proc. IEEE Int. Conf. Microelectron. Test Structures*, 2007, pp. 55–58.

[13] Y. Mitsui, T. Sunaoshi, and J. C. Lee, "A study of electrical characteristic changes in MOSFET by electron beam irradiation," *Microelectron. Rel.*, vol. 49, no. 9, pp. 1182–1187, 2009.

[14] X. Ye, Y. Zhang, C. Ru, J. Luo, S. Xie, and Y. Sun, "Automated pick-place of silicon nanowires," *IEEE Trans. Autom. Sci. Eng.*, vol. 10, no. 3, pp. 554–561, Jul. 2013.

[15] S. Fatikow, V. Eichhorn, D. Jasper, M. Weigel-Jech, F. Niewiera, and F. Krohs, "Automated nanorobotic handling of bio- and nano-materials," in *Proc. IEEE Conf. Autom. Sci. Eng.*, 2010, pp. 1–6.

[16] C. Stolle, M. Bartenwerfer, C. Celle, J. Simonato, and S. Fatikow, "Nanorobotic strategies for handling and characterization of metal-assisted etched silicon nanowires," *IEEE/ASME Trans. Mechatronics*, vol. 18, no. 3, pp. 887–894, Jun. 2013.

[17] Y. L. Zhang, J. Li, S. To, Y. Zhang, X. Ye, L. You, and Y. Sun, "Automated nanomanipulation for nanodevice construction," *Nanotechnology*, vol. 23, no. 6, p. 065304, 2012. Available: http://iopscience.iop.org/0957-4484/23/6/065304/pdf/0957-4484_23_6_065304.pdf.

[18] Y. Shen, M. Nakajima, P. Di, T. Yue, S. Kojima, M. Homma, and T. Fukuda, "Development of the auto manipulation system towards the single cell automatic analysis inside an environmental sem," in *Proc. IEEE Int. Conf. Robot. Autom.*, 2012, pp. 4594–4599.

[19] J. Portilla, V. Strela, M. Wainwright, and E. Simoncelli, "Image denoising using scale mixtures of Gaussians in the wavelet domain," *IEEE Trans. Image Process.*, vol. 12, no. 11, pp. 1338–1351, Nov. 2003.

[20] S. M. Smith and J. M. Brady, "Susana new approach to low level image processing," *Int. J. Comput. Vis.*, vol. 23, no. 1, pp. 45–78, 1997.

[21] F. Catté, P.-L. Lions, J.-M. Morel, and T. Coll, "Image selective smoothing and edge detection by nonlinear diffusion," *SIAM J. Numer. Anal.*, vol. 29, no. 1, pp. 182–193, 1992.

[22] C. R. Vogel and M. E. Oman, "Iterative methods for total variation denoising," *SIAM J. Sci. Comput.*, vol. 17, no. 1, pp. 227–238, 1996.

[23] N. Ouarti, B. Sauvet, and S. Régnier, "High quality real-time video with scanning electron microscope using total variation algorithm on a graphics processing unit," *Int. J. Optomechatronics*, vol. 6, no. 2, pp. 163–178, 2012.

[24] A. Buades, B. Coll, and J.-M. Morel, "A non-local algorithm for image denoising," in *Proc. IEEE Comput. Soc. Conf. Comput. Vis. Pattern Recog.*, 2005, vol. 2, pp. 60–65.

[25] P. Cizmar, A. E. Vladár, and M. T. Postek, "Real-time scanning charged-particle microscope image composition with correction of drift," *Microscopy Microanal.*, vol. 17, no. 2, pp. 302–308, 2011.

[26] M. Sutton, N. Li, D. Joy, A. Reynolds, and X. Li, "Scanning electron microscopy for quantitative small and large deformation measurements part i: Sem imaging at magnifications from 200 to 10,000," *Exp. Mech.*, vol. 47, no. 6, pp. 775–787, 2007.

[27] S. Belikov, J. Shi, and C. Su, "AFM image based pattern detection for adaptive drift compensation and positioning at the nanometer scale," in *Proc. Am. Control Conf.*, 2008, pp. 2046–2051.

[28] S. Chang, C. S. Wang, C. Y. Xiong, and J. Fang, "Nanoscale in-plane displacement evaluation by AFM scanning and digital image correlation processing," *Nanotechnology*, vol. 16, no. 4, pp. 344–349, 2005.

[29] Z. Gong, B. K. Chen, J. Liu, and Y. Sun, "Automated nanoprobing under scanning electron microscopy," in *Proc. IEEE Int. Conf. Robot. Autom.*, May 2013, pp. 1433–1438.

[30] Y. L. Zhang, Y. Zhang, C. Ru, B. K. Chen, and Y. Sun, "A load-lock-compatible nanomanipulation system for scanning electron microscope," *IEEE/ASME Trans. Mechatronics*, vol. 18, no. 1, pp. 230–237, 2011.
[31] C. Ru, Y. Zhang, Y. Sun, Y. Zhong, X. Sun, D. Hoyle, and I. Cotton, "Automated four-point probe measurement of nanowires inside a scanning electron microscope," *IEEE Trans. Nanotechnol.*, vol. 10, no. 4, pp. 674–681, Jul. 2011.
[32] B. D. Lucas and T. Kanade, "An iterative image registration technique with an application to stereo vision," in *Proc. 7th Int. Joint Conf. Artif. Intell.*, 1981, vol. 2, pp. 674–679.
[33] A. Buades, B. Coll, and J. M. Morel, "A review of image denoising algorithms, with a new one," *Multiscale Modeling Simul.*, vol. 4, no. 2, pp. 490–530, 2005.
[34] J. Sanders and E. Kandrot, *CUDA by Example: An Introduction to General-Purpose GPU Programming*, 1st ed. Reading, MA, USA: Addison-Wesley, 2010.
[35] F. Goudail and P. Réfrégier, *Statistical Image Processing Techniques for Noisy Images: An Application-Oriented Approach*. Norwell, MA, USA: Kluwer, 2004.

Natural Gaits for Multilink Mechanical Systems

Md Nurul Islam and Zhiyong Chen

***Abstract*—Typical animal locomotion is achieved by the rhythmical undulation of its body segments while interacting with its environment. It inspires the mechanical design of multilink locomotors. With different postures, a multilink system may present different locomotion gaits. Recently, a so-called natural oscillation gait was studied for multilink systems, and a class of biologically inspired controllers was designed for the achievement of the gait. In this paper, the theoretical design is experimentally applied on a mechanical multilink testbed of two posture configurations in rayfish-like flapping-wing motion and snake-like serpentine motion. The effectiveness of the design is cross examined by theoretical analysis, numerical simulation, and experiments.**

***Index Terms*—Biologically inspired control, central pattern generator (CPG), locomotion, robotics.**

I. Introduction

Research on biologically inspired robotics, especially multilink snake robots, is of constant interest for biologists and engineers. Analytical studies of snake locomotion as a multisegmental system can be traced back to Gray's work [1], which emphasized the importance of environmental forces acting in the normal direction during body undulation. A recent review on snake robots was given in [2], which considers research efforts that are related to modeling of snake robots, physical development, and control design for snake locomotion. From the literature over the past decades, research on snake robots was conducted along a variety of research lines. One of the main research lines focuses on structural development for new functionalities. For example, the robots in "active cord mechanism" developed in Hirose's group have "the function of an arm" when they hold something by rolling itself and have "the function of legs" when they move by creeping (see, e.g., [3] and [4]). The modular snake robots designed in Choset's group are able to use their many degrees of freedom (DOFs) to achieve a variety of locomotion capabilities like searching across a gap, traversing through brush, swimming, and climbing inside and outside a pipe (see, e.g., [5] and [6]). The curvature-derivative-based robots designed by Date and Takita [7] are able to adaptively travel over rugged terrain using obstacles as supports. A similar idea was used in the Kano *et al.* design [8]. Their snakes actively utilize terrain irregularities and move by effectively pushing their body against the scaffolds that they encounter. The adaptability to environment was analyzed in [9] for a class of snake-like robot using passive creeping.

Another research line aims to understand and design rhythmic patterns of body oscillation to generate robot locomotion. For example, in [10] and [11], snake-like locomotors were regulated to achieve sinusoidal set points characterized by amplitudes, frequencies, and phase lags. The central pattern generator (CPG) is an important concept widely used in this direction. A CPG is a group of neurons interconnected in a specific manner, which can endogenously produce rhythmic outputs to activate muscle contractions, resulting in coordinated rhythmic body motions. A CPG-based controller was used in [12] to generate traveling waves in terms of asymptotically stable limit cycle trajectories. It was also used in [13], where the relation between the CPG parameters and the serpentine locomotion was defined. Many other CPG-based controllers can be found in the literature, e.g., for snake robots [14], [15] and for turtle-like underwater vehicles [16]. In the aforementioned sine-based or CPG-based architecture, the rhythmic patterns of body oscillation are designed for specific applications. It is interesting to develop general approaches to select rhythmic patterns for a locomotor, typically based on its kinematic or dynamic model. Such models have been widely studied in the literature, e.g., [17] for serpentine locomotion, [18] for 3-D snake robots, and [19] for general flexible link manipulators. Based on the models, a variety of rhythmic patterns have been studied. The feature of these rhythmic patterns is that they are entrained with the physical system; hence, if the system parameters change, the patterns can change accordingly (in comparison with approaches where the patterns are generated in open-loop manner and with neural coupling rather than mechanical coupling). The most recent results include the optimal gait proposed in [20] and the natural oscillation gait in [21] and [22].

This paper follows the theoretical framework for the natural oscillation proposed in [21] and [22]. In particular, natural oscillation is an inherent characteristic of a mechanical rectifier interacting with environment, which is defined as the free response in persistent oscillation of the system with its damping properly compensated. The concept is consistent with the well-established one for standard lightly damped mechanical systems (like a pendulum), which is defined to be a free response of the modified system that is obtained by removing all the damping effects to achieve marginal stability for sustained oscillation. The main objective of this paper is to experimentally verify that the so-called natural oscillation does exist in real multilink mechanical systems, and it can be effectively achieved in a locomotion behavior. Actually, a simpler testbed, called the prototype mechanical rectifier (PMR), has been established in our recent work [23] to experimentally verify the theoretical framework. The PMR system consists of two main parts: a double pendulum and a disk. The intended operation of the PMR is basically to swing the pendulum in a coordinated manner to make the disk rotate. The PMR model is simple enough to allow us to extract engineering principles by theoretical analysis, simulation, and experiments; however, because of the simple structure of the PMR model, complicated locomotion behaviors cannot be demonstrated. In this paper, we focus on a more sophisticated structure, which is used as the experimental platform to

Manuscript received April 16, 2013; revised October 8, 2013; accepted January 6, 2014. Date of publication January 28, 2014; date of current version June 3, 2014. This paper was recommended for publication by Associate Editor J. Peters and Editor G. Oriolo upon evaluation of the reviewers' comments. This work was supported in part by the Australian Research Council under Grant DP130103039 and in part by the National Natural Science Foundation of China under Grant 51328501. *(Corresponding author: Z. Chen).*

The authors are with the School of Electrical Engineering and Computer Science, the University of Newcastle, Callaghan, NSW 2308, Australia (e-mail: md.n.islam@uon.edu.au; zhiyong.chen@newcastle.edu.au).

Color versions of one or more of the figures in this paper are available online at http://ieeexplore.ieee.org.

Digital Object Identifier 10.1109/TRO.2014.2298926